COMPRESSIVE BUCKLING STRENGTH OF GRAPHITE-EPOXY LAMINATED CURVED PANELS

ICAS-86-4.2.2

Shigeo KOBAYASHI, Kiyohide SUMIHARA and Kazuo KOYAMA

Department of Aeronautics, University of Tokyo
Hongo 7, Bunkyo-ku, Tokyo, JAPAN

Abstract

The post-buckling behavior of graphite-epoxy curved plates under compressive load has been studied by experiments, the Galerkin method and the finite element method. Panels of seven types of lamination constitution have been treated, and the influence of lamination constitution on the behavior has been disclosed.

1. Introduction

For graphite-epoxy flat panels, the authors have studied on its post-buckling behavior under compressive load or shearing load by theoretical analyses and experiments and have demonstrated its load carrying capability at the post-buckling state.[1)~4)] In the present paper, as an advanced study, the post-buckling behavior of graphite-epoxy curved panels under compressive load is studied by experiments, the Galerkin method and the FEM analysis, and the influence of lamination constitution on the behavior is disclosed.

For the post-buckling behavior of curved panels, although several studies, for example the references 5) and 6), have been presented for isotropic materials, Zhang and Matthew's analytical study by the Galerkin method about the simply supported panels is only one paper for the laminates.[7)] For the compressive buckling load of graphite-epoxy circular cylindrical shells, one of the authors has disclosed that the quasi-isotropic lamination constitution is optimum, if the elastic properties are homogeneous in thicknesswise.[8),9)] Therefore, as the lamination constitution of the test specimens, the one which becomes quasi-isotropic if the number of layers is infinite and the others which are composed of 0°, 90° and ±45° layers are selected.

2. Approximate Analysis by the Galerkin Method

2.1 Expressions of One-Term Approximate Solution

The fundamental equations of a circular cylindrical curved plate without initial imperfection in the large deflection theory is expressed as

$$D_{xx}W_{,xxxx} + 2(D_{xy}+2D_{ss})\cdot W_{,xxyy} + D_{yy}W_{,yyyy} + F_{,xx}/R - F_{,yy}W_{,xx} - F_{,xx}W_{,yy} + 2F_{,xy}W_{,xy} = 0 \quad (1)$$

$$a_{22}F_{,xxxx} + (2a_{12}+a_{33})\cdot F_{,xxyy} + a_{11}F_{,yyyy} = W_{,xx}/R + (W_{,xy})^2 - W_{,xx}W_{,yy} \quad (2)$$

for the symmetrical laminates in the use of the radial displacement W and the middle surface stress function F (see Fig.1). The definition of elastic moduli of symmetrical laminates is as follows:

$$[A_{ij}, D_{ij}] = \sum_{m=1}^{n} \int_{t_{m-1}}^{t_m} [1, z^2] E_{ij}^{(m)}\, dz, \quad (i,j=x,y,s) \quad (3)$$

$$[a] = [A]^{-1} \quad (4)$$

We take the following boundary conditions in this section:

$$x = \pm b/2 \ ; \ W = 0 \ , \ W_{,x} = 0 \ , \ N_{xy} = -F_{,xy} = 0 \ , \ u = \text{const.} \quad (5)$$

$$y = \pm b/2 \ ; \ W = 0 \ , \ W_{,yy} = 0 \ , \ N_{xy} = -F_{,xy} = 0 \ , \ N_y = F_{,xx} = 0 \quad (6)$$

The conditions except Nxy=0 at x=±b/2 are regarded as the same with those of the present expriment. Although the boundary condition is rather regarded as v=0 at x=±b/2 instead of Nxy=0, we can easily obtain one-mode approximate solution to satisfy the boundary condition (5) and (6) as follows.

We use

$$W = W_1 \ [1+\cos(2\pi x/b)]\cdot\cos(\pi y/b) \quad (7)$$

as an expression of deflection which satisfies the boundary conditions for deflection. Substituting Eq.(7) into the right hand side of Eq.(2), we get the particular solution

$$F_p = -t\sigma_1 y^2/2 - [4b^2W_1/(\pi^2 R f_1)]\cos(2\pi x/b)\cos(\pi y/b) - (W_1^2/8)\{[1/(16a_{22})]\cos(4\pi x/b) + (1/a_{22})\cos(2\pi x/b) + (1/a_{11})\cos(2\pi y/b) + (1/f_2)\cos(2\pi x/b)\cos(2\pi y/b)\} \quad (8)$$

where

$$f_1 = 16a_{22} + 4(2a_{12}+a_{33}) + a_{11}\ ,$$

$$f_2 = a_{22} + (2a_{12}+a_{33}) + a_{11}$$

and σ_1 is the mean compressive stress. In order to obtain the solution of the homogeneous equation of Eq.(2), substituting

$$F(x,y) = \cos(m\pi x/b)\exp(\lambda y) \qquad (m: \text{integer}) \quad (9)$$

which satisfies the boundary condition F,xy=0 at x=±b/2 into the equation, we can derive the characteristic equation which is quadratic for λ^2. The roots of the equation are

$$\mu^2 = [b\lambda/(m\pi)]^2 = \{1/(2a_{11})\}[(2a_{12}+a_{33}) \pm \{(2a_{12}+a_{33})^2 - 4a_{11}a_{22}\}^{1/2}] \quad (10)$$

Therefore the pattern of the solution is classified into three types according to the property of μ as follows.

(1) The case of $(2a_{12}+a_{33})^2 - 4a_{11}a_{22} > 0$.

We get $\mu = \pm\mu_1$ and $\pm\mu_2$, where μ_1 and μ_2 are real positive. Taking into account the symmetric property for the x axis and the form of Fp for x,

we have the expression of Fh

$$F_h = \cos(2\pi x/b)\cdot[A_1\cosh(2\pi\mu_1 y/b) + A_2\cosh(2\pi\mu_2 y/b)] + \cos(4\pi x/b)\cdot[C_1\cosh(4\pi\mu_1 y/b) + C_2\cosh(4\pi\mu_2 y/b)] \quad (11)$$

where the constants A_1, A_2, C_1, and C_2 are determined by the boundary conditions (Fp+Fh),xy=0 and (Fp+Fh),xx=0 at y=b/2 for any x. Substituting F=Fp+Fh and W of Eq.(7) into

$$\partial u/\partial x = a_{11}F,yy + a_{12}F,xx - (W,x)^2/2 \quad (12)$$

and integrating by x from -b/2 to b/2, we get the expression of end shortening

$$Ues = [u]_{-b/2}^{b/2} = -a_{11}\sigma_1 bt - \pi^2 W_1^2/(2b) \quad (13)$$

which is independent of y.

Substituting Eq.(7) for W and Eqs.(8) and (11) for F into the left hand side of Eq.(1), and writing is as $\Phi[W_1]$, we take

$$\int_{-b/2}^{b/2}\int_{-b/2}^{b/2} \Phi[W_1]\cdot\{1+\cos(2\pi x/b)\}\cos(\pi y/b)\,dxdy = 0 \quad (14)$$

instead of Eq.(1) by the Galerkin method. The calculation of Eq.(14) yields the equation of equilibrium curve between the load $P=\sigma_1 tb$ and W_1:

$$A W_1^3 + B W_1^2 + C W_1 = 0 \quad (15)$$

where

$$A = \{\pi^4/(8b^2)\}\cdot\{2/a_{11}+17/(8a_{22})+1/f_2\} - \{\pi^3/(4b^2)\}\times[\sinh\pi\mu_1\sinh\pi\mu_2/(\mu_2\cosh\pi\mu_1\sinh\pi\mu_2 - \mu_1\sinh\pi\mu_1\cosh\pi\mu_2)]\cdot(1/a_{22}-1/f_2)\cdot\{\mu_2^2(1+\mu_2^2)-\mu_1^2(1+\mu_1^2)\}/\{\mu_1\mu_2(1+\mu_1^2)\times(1+\mu_2^2)\} + \{1/(128a_{11})\}[\sinh2\pi\mu_1\sinh2\pi\mu_2/(\mu_2\cosh2\pi\mu_1\times\sinh2\pi\mu_2 - \mu_1\sinh2\pi\mu_1\cosh2\pi\mu_2)](\mu_2^2-\mu_1^2)/(\mu_1\mu_2)$$

$$B = (\pi/R)\{1/(2a_{22})+1/(6f_2)+64/(3f_1)\} - (\pi/R)/(\mu_2\cosh\pi\mu_1\times\sinh\pi\mu_2 - \mu_1\sinh\pi\mu_1\cosh\pi\mu_2)\cdot[\{(1/a_{22}-1/f_2)/2\}\cdot\{\mu_2(1+4\mu_2^2)\sinh\pi\mu_2\cosh\pi\mu_1 - \mu_1(1+4\mu_1^2)\sinh\pi\mu_1\cosh\pi\mu_2\}/\{(1+4\mu_1^2)(1+4\mu_2^2)\} + (4/f_1)\cdot\{\mu_2(1+\mu_2^2)\sinh\pi\mu_1\cosh\pi\mu_2 - \mu_1(1+\mu_1^2)\sinh\pi\mu_2\cosh\pi\mu_1\}/\{\mu_1\mu_2(1+\mu_1^2)(1+\mu_2^2)\}]$$

$$C = (\pi^4/b^2)\cdot\{4Dxx+2(Dxy+2Dss)+3Dyy/4\} + 4b^2/(R^2f_1) - \pi^2\sigma_1 t - \{8b^2/(\pi R^2 f_1)\}\{\cosh\pi\mu_1\cosh\pi\mu_2/(\mu_2\cosh\pi\mu_1\sinh\pi\mu_2 - \mu_1\sinh\pi\mu_1\cosh\pi\mu_2)\}4(\mu_2^2-\mu_1^2)/\{(1+4\mu_1^2)(1+4\mu_2^2)\} \quad (16)$$

If the effective width b_m is defined by

$$\sigma_1 bt = -Ues\, b_m\, t/(a_{11}bt) \quad (17)$$

as in the case of the flat panel, substitution of Eq.(13) yields a formula

$$b_m/b = 1/[1+\pi^2 W_1^2/(2a_{11}b^2 t\sigma_1)] \quad (18)$$

(2) The case of $(2a_{12}+a_{33})^2 - 4a_{11}a_{22}=0$

As the characteristic value is $\mu_1=\mu_2=1$, the expression of Fh becomes a different form from Eq.(11) essentially. However, putting as $\mu_2=\mu_1+\varepsilon$ and taking the limit $\varepsilon\to 0$, we can derive

$$A = \{\pi^4/(8b^2)\}\{2/a_{11}+17/(8a_{22})+1/f_2\} - \{3\pi^3/(8b^2)\}\times(1/a_{22}-1/f_2)(\sinh\pi)^2/(\cosh\pi\sinh\pi+\pi) + \{1/(64a_{11})\}\times(\sinh2\pi)^2/(\cosh2\pi\sinh2\pi+2\pi)$$

$$B = (\pi/R)\{1/(2a_{22})+1/(6f_2)+64/(3f_1)\} - \{(\pi/R)/(\cosh\pi\sinh\pi+\pi)\}\{(1/a_{22}-1/f_2)/50\}(13\sinh\pi\cosh\pi + (2/f_1)(2\sinh\pi\cosh\pi-\pi)\}$$

$$C = (\pi^4/b^2)\{4Dxx+2(Dxy+2Dss)+3Dyy/4\} + 4b^2/(R^2f_1) - \pi^2\sigma_1 t - \{64b^2/(25\pi R^2 f_1)\}(\cosh\pi)^2/(\cosh\pi\sinh\pi+\pi) \quad (19)$$

as the expression of the coefficients of Eq.(15).

(3) The case of $(2a_{12}+a_{33})^2 - 4a_{11}a_{22}<0$.

As the four roots μ become complex variables $\pm\mu_1+i\mu_2$, we take the following expression of homogeneous solution:

$$F_h = \cos(2\pi x/b)[A_1\sinh(2\pi\mu_1 y/b)\sin(2\pi\mu_2 y/b) + A_2\cosh(2\pi\mu_1 y/b)\cos(2\pi\mu_2 y/b)] + \cos(4\pi x/b)[C_1\sinh(4\pi\mu_1 y/b)\sin(4\pi\mu_2 y/b) + C_2\cosh(4\pi\mu_1 y/b)\cos(4\pi\mu_2 y/b)] \quad (20)$$

where the constants A_1, A_2, C_1 and C_2 are determined by the boundary conditions as mentioned above. Finally the expression of the coefficients of Eq.(15) is obtained as

$$A = \{\pi^4/(8b^2)\}\{2/a_{11}+17/(8a_{22})+1/f_2\} - (b\alpha^4/4)[-2\alpha_2\times\{(\mu_1^2-\mu_2^2)I_1+2\mu_1\mu_2 I_2\} - 2\alpha_4\{(\mu_1^2-\mu_2^2)I_2 - 2\mu_1\mu_2 I_1\} - 4\beta_1\{(\mu_1^2-\mu_2^2)I_3+2\mu_1\mu_2 I_4\} - 4\beta_2\{(\mu_1^2-\mu_2^2)I_4 - 2\mu_1\mu_2 I_3\} + \alpha_2 I_1 + \alpha_4 I_2 + \beta_1 I_3 + \beta_2 I_4 + 2\alpha_2(\mu_1 I_5+\mu_2 I_6) + 2\alpha_4(\mu_1 I_6 - \mu_2 I_5) + 4\beta_1(\mu_1 I_7+\mu_2 I_8) + 4\beta_2(\mu_1 I_8 - \mu_2 I_7)]$$

$$B = (\pi/R)\{1/(2a_{22})+1/(6f_2)+64/(3f_1)\} - (b\alpha^4/4)[2(\alpha_2 I_9 + \alpha_4 I_{10})/(R\alpha^2) - 2\alpha_1\{(\mu_1^2-\mu_2^2)I_1+2\mu_1\mu_2 I_2\} - 2\alpha_3\{(\mu_1^2-\mu_2^2)I_2 - 2\mu_1\mu_2 I_1\} + \alpha_1 I_1 + \alpha_3 I_2 + 2\alpha_1(\mu_1 I_5+\mu_2 I_6) + 2\alpha_3(\mu_1 I_6 - \mu_2 I_5)]$$

$$C = (\pi^4/b^2)\cdot\{4Dxx+2(Dxy+2Dss)+3Dyy/4\} + 4b^2/(R^2f_1) - \pi^2\sigma_1 t - \{b\alpha^2/(2R)\}(\alpha_1 I_9 + \alpha_3 I_{10}) \quad (21)$$

where

$$\alpha = 2\pi/b$$

$$I_1 = \int_{-b/2}^{b/2}\sinh\alpha\mu_1 y\sin\alpha\mu_2 y\{\cos(\alpha y/2)\}^2 dy$$

$$I_2 = \int_{-b/2}^{b/2}\cosh\alpha\mu_1 y\cos\alpha\mu_2 y\{\cos(\alpha y/2)\}^2 dy$$

$$I_3 = \int_{-b/2}^{b/2}\sinh2\alpha\mu_1 y\sin2\alpha\mu_2 y\{\cos(\alpha y/2)\}^2 dy$$

$$I_4 = \int_{-b/2}^{b/2}\cosh2\alpha\mu_1 y\cos2\alpha\mu_2 y\{\cos(\alpha y/2)\}^2 dy$$

$$I_5 = \int_{-b/2}^{b/2}\cosh\alpha\mu_1 y\sin\alpha\mu_2 y\cos(\alpha y/2)\sin(\alpha y/2)dy$$

$$I_6 = \int_{-b/2}^{b/2}\sinh\alpha\mu_1 y\cos\alpha\mu_2 y\cos(\alpha y/2)\sin(\alpha y/2)dy$$

$$I_7 = \int_{-b/2}^{b/2}\cosh2\alpha\mu_1 y\sin2\alpha\mu_2 y\cos(\alpha y/2)\sin(\alpha y/2)dy$$

$$I_8 = \int_{-b/2}^{b/2}\sinh2\alpha\mu_1 y\cos2\alpha\mu_2 y\cos(\alpha y/2)\sin(\alpha y/2)dy$$

$$\alpha_1 = -2b^2\cosh\pi\mu_1\cos\pi\mu_2/(\pi^2 R f_1 W_a)$$

$$\alpha_2 = -(1/a_{22}-1/f_2)\cdot(\mu_1\sinh\pi\mu_1\cos\pi\mu_2 - \mu_2\cosh\pi\mu_1\sin\pi\mu_2)/(8W_a)$$

$$\alpha_3 = 2b^2 \sinh\pi\mu_1 \sin\pi\mu_2 / (\pi^2 R f_1 W_a)$$

$$\alpha_4 = (1/a_{22} - 1/f_2)\cdot(\mu_1 \cosh\pi\mu_1 \sin\pi\mu_2 + \mu_2 \sinh\pi\mu_1 \cos\pi\mu_2) / (8W_a)$$

$$\beta_1 = -(\mu_1 \sinh 2\pi\mu_1 \cos 2\pi\mu_2 - \mu_2 \cosh 2\pi\mu_1 \sin 2\pi\mu_2) / (128 a_{22} W_c)$$

$$\beta_2 = (\mu_1 \cosh 2\pi\mu_1 \sin 2\pi\mu_2 + \mu_2 \sinh 2\pi\mu_1 \cos 2\pi\mu_2) / (128 a_{22} W_c)$$

$$W_a = \mu_1 \sin\pi\mu_2 \cos\pi\mu_2 + \mu_2 \sinh\pi\mu_1 \cosh\pi\mu_1$$

$$W_c = \mu_1 \sin 2\pi\mu_2 \cos 2\pi\mu_2 + \mu_2 \sinh 2\pi\mu_1 \cosh 2\pi\mu_1 \qquad (22)$$

2.2 Analytical Results

As a numerical example, the values of all test specimens, whose lamination constitution is shown in Tabel 1, are treated. The elastic moduli of unidirectional graphite-epoxy composites shown in Table 2-B have been calculated for Vf=60% from the elastic moduli of the fiber and the matrix written in the reference 10), which is also shown in Table 2-A, through the method of the reference 11). The elastic moduli aij and Dij of each test laminates are calculated from the value of Table 2B and are shown in Table 3. The characteristic values μ of each test panel are shown in Table 4. The test panels 6p-1 and 8p-2 correspond to the case (1), the in-plane quasi-isotropic test panels 6p-2, 6p-3, 8p-1 and 12p-1 correspond to the case (2) and the test panel 8p-3 corresponds to the case (3).

The relation between the load $P=\sigma_1 bt$ and the end shortening Ues shown in Figs.2a~2b is similar as the well-known curves for isotrpic materials. The upper and the lower curves correspond to $W_1>0$ and $W_1<0$, respectively. These figures suggest the possibility of snap-through from the upper curve to the lower curve in the experiment controlling the end-shortening. Specimens 6p-2 and 6p-3 have the same in-plane elastic moduli essentially, but have the different out-of-plane elastic moduli depending on the difference of the stacking sequence, which yields the difference of the buckling load. Clear differences are seen among the properties of three kinds of panels with eight-layers. Although the panel 8p-2 has the highest compressive rigidity, the buckling load is lower than those of 8p-1 and 8p-3. The compressive rigidity of 8p-3 is very low. The property that the buckling load of the in-plane quasi-isotropic panel is higher than that of others is the same as that of the cylindrical shell.[3),9)]

Figs.3a and 3b show the relation between the effective width ratio bm/b and the load ratio P/Pcr, where Pcr means the buckling load. For the equilibrium curve of $W_1<0$, the value of bm/b is less than about 0.6 at P/Pcr=1 already, and there is no distinct decrease with the increase of P/Pcr except the panels 6p-1 and 8p-2.

The P/Pcr(plate) versus Wc/t relation is shown in Fig.4. Pcr(plate) means the buckling load of the flat plate with the same boundary condition and stacking sequence. Wc means the deflection of the center point positive in the concave side, namely is equal to $-2W_1$. The intersection of the curve with the ordinate is the buckling load of the curved panel. Comparing the properties of panels stiffened in 0° and 90° directions, namely 6p-2 and 8p-1, with those of the in-plane quasi-isotropic panels in the condition of about the same value of shape parameter $Z=b^2/(Rt)$, we can observe the following properties: 1) the rate of increase of the buckling load by curvature is lower, 2) the drop of the minimum point of P/Pcr(plate) from the buckling load is lower, 3) the value of Wc/t which gives the above-mentioned minimum point is smaller, and the rate of increase of P/Pcr(plate) at the Wc/t larger than the minimum point is higher.

The buckling load by the Galerkin method shown in Table 1 is calculated from

$$P = \sigma_1 bt + E_x Ues 2\ell t/b \qquad (b=120mm, \ell=8mm) \qquad (23)$$

including the correction of the load carrying capability of two edge strips whose width ℓ=8mm at $|y|>b/2$, for comparison with experiment.

2.3 Buckling Property of 6p-3 Panel

The FEM analysis of the section 4 has yielded that the buckling mode of the panel "6p-3" is different from Eq.(7) and includes higher modes. Then, assuming an expression of higher mode.

$$W = W_1 \{1-\cos(4\pi x/b)\}\cos(\pi y/b) \qquad (24)$$

and using linearized equations of Eqs.(1). and (2), and applying the Galerkin method, we can obtain the expression of buckling load

$$Nx = -(\pi^2/b^2)\{16Dxx + 2(Dxy + 2Dss) + 3Dyy/16\} - 16b^2/[\pi^2 R^2 (256a_{22} + 16(2a_{12} + a_{33}) + a_{11})] \qquad (25)$$

Including the load capability of the edge strips, we get $Pcr=-Nx\cdot(b+2\ell)=401kgf$, which is lower than Pcr=464kgf calculated from the mode of Eq.(7). This result is mainly due to the property that Dyy is greater than Dxx as shown in Table 3.

3. Experiment

3.1 Procedure of Experiment

Compressive tests were carried out about curved panels of seven types of stacking sequence shown in Table 1. The specimens were made by TORAY Inc. in hot-press curring of lamination of unidirectional prepreg sheets of about 0.12mm thickness. The graphite fiber is Torayca T300 and the epoxy regin is #2500. The volume fraction of the fiber of the specimens is about 60%. The numbers of layers of the sheet are three kinds, namely six, eight and twelve. The radius of curvature R is 500mm. The size of the specimen is 170mm in longitudinal length including the parts of upper and lower fixtures and is 136mm in the arch length including both edge strips. The test part is a square of b=120mm.

The figure of the test apparatus is shown in Fig.5 . The load was applied by Instron testing machine in crosshead speed 0.05cm/min.. The center of load was adjusted so as to coincide with the center of the section of the panel. The panel was fixed to the upper and lower fixtures with bolts and a low melting point metal, i.e. TU-60, so as to make the condition of clamp for both in-plane and out-of-plane as shown in Fig.5 . The line which is 8mm from the side edge is supported by a rod of high strength steel with a circular cross-section of diameter 10mm. The clamping force of the rod was adjusted so as to make the boundary condition which is simply supported for out-of-plane and free for the inplane direction through

the checking of the strain distribution by wire strain gauges. The thirty-six strains at the points and directions shown in Fig.6 were measured. Displacement was measured at the four points shown in Fig.5a. The gages at the points 0 and 2 indicate the center deflection and the end-shortening, respectively. The measurements at the points 1 and 3 were only for the porpose of checking the test accuracy.

3.2 Test Results

The experimental maximum load and snap-through load are listed in Table 1. The load versus center deflection relation and the load versus end-shortening relation of each test results are shown in Figs.7~13. In the tests except 8p-2 and 12p-1, the snap-through from the convex side deflection to the concave side one occurred before the maximum load. In the tests 6p-1, 6p-3, 8p-3Ⅰ and 8p-3Ⅱ, the decrease of convex side deflection were seen before the snap-through. However, in the tests 6p-2 and 8p-1 the snap-through occurred abruptly. In the test12p-1, after the load dropped from the maximum by local failure in the convex side deflection, a snap-through to the concave side occurred, but in the concave side the load did not increase under the increase of end-shortening.

In the tests 6p-1, 8p-3Ⅰ and 8p-3Ⅱ, the end-shortening was removed after observation of snap-through before the final failure test. In other tests the loading is one process until the failure. In Table 5 the maximum values of tensile strains and compressive strains among all strain gages at the load written in Table 5 are listed with the number of gage in parentheses.

Except the test 8p-3Ⅰ, 8p-3Ⅱ and 8p-2, the failure occurred at the region which is close to edge and a little bit higher than the middle as shown in Photograph 1. At the failure point the peeling of the surface layer was observed. After removing the panel from the test set-up, a interlamina peeling was observed at the free edge in most of test specimen. In the test 8p-3Ⅰ and 8p-3Ⅱ cracks of 45° direction appeared at the both side edge lines at the point about b/4 lower from the upper loading edge as shown in Photograph 2. In the test 8p-3Ⅱ the crack penetrated from one surface to the other surface.

The failure mode of 8p-2 is quite different from the others as shown in Photograph 3. The crack line is nearly parallel to the lower edge and about 27mm upper from the lower edge. The crack penetrated from surface to surface. After removing the panel from the test set-up it was observed that the panel was completely separated into two parts and the failure surface was skew to the panel surface.

4. Analysis by Finite Element Method

4.1 Method of Analysis

A hybrid method for a plate element which was derived by the authors in the reference 2) has been used. The curved plate is divided into rectangular curved elements as shown in Fig.14 . The each curved element, as it is shallow, is treated as a plate element with initial imperfection in the local flat coordinate system through the four corner nodal points. The initial imperfection shape is treated as a quadratic curve which goes through the point of maximum rise. In the element with four corner nodal points, the degrees of freedom of each nodal point are u_ξ, u_η, u_ζ, θ_ξ and θ_η , and the interporation function of displacement of inner points is

$$\{u_\xi, u_\eta\}^T = \sum_{i=1}^{4} N_i(\xi,\eta)\{u_{\xi_i}, u_{\eta_i}\}^T$$
$$u_\zeta = \sum_{i=1}^{4} (N_i^W w_i + N_i^\theta{}_\xi(\theta_\xi)_i + N_i^\theta{}_\eta(\theta_\eta)_i) \quad (26)$$

where

$$N_1 = (1-\xi)(1-\eta)\ ,\ N_2 = \xi(1-\eta)\ ,\ N_3 = \xi\eta\ ,\ N_4 = (1-\xi)\eta$$
$$N_1^W = M_1(\xi)M_1(\eta)\ ,\ N_1^\theta{}_\xi = M_1(\xi)M_3(\eta)\ ,\ N_1^\theta{}_\eta = M_3(\xi)M_1(\eta)$$
$$N_2^W = M_2(\xi)M_1(\eta)\ ,\ N_2^\theta{}_\xi = M_2(\xi)M_3(\eta)\ ,\ N_2^\theta{}_\eta = M_4(\xi)M_1(\eta)$$
$$N_3^W = M_2(\xi)M_2(\eta)\ ,\ N_3^\theta{}_\xi = M_2(\xi)M_4(\eta)\ ,\ N_3^\theta{}_\eta = M_4(\xi)M_2(\eta)$$
$$N_4^W = M_1(\xi)M_2(\eta)\ ,\ N_4^\theta{}_\xi = M_1(\xi)M_4(\eta)\ ,\ N_4^\theta{}_\eta = M_3(\xi)M_2(\eta)$$
$$M_1(\xi) = 1+2\xi^3-3\xi^2\ ,\ M_1(\eta) = 1+2\eta^3-3\eta^2$$
$$M_2(\xi) = 3\xi^2-2\xi^3\ ,\ M_2(\eta) = 3\eta^2-2\eta^3$$
$$M_3(\xi) = -a\xi(\xi-1)^2\ ,\ M_3(\eta) = b\eta(\eta-1)^2$$
$$M_4(\xi) = -a\xi(\xi^2-\xi)\ ,\ M_4(\eta) = b\eta(\eta^2-\eta) \quad (27)$$

and $\xi = x/a, \eta = y/b$, where a and b are the edge length of rectangular element in x and y directions, respectively.

The expressions of stress field in the element are assumed as

$$N_\xi = \beta_1+\beta_2\eta\ ,\ N_\eta = \beta_3+\beta_4\xi\ ,\ N_{\xi\eta} = \beta_5$$
$$M_\xi = \beta_6+\beta_7\xi+\beta_8\eta+\beta_9\xi\eta\ ,\ M_\eta = \beta_{10}+\beta_{11}\xi+\beta_{12}\eta+\beta_{13}\xi\eta\ , \quad (28)$$
$$M_{\xi\eta} = \beta_{14}+\beta_{15}\xi+\beta_{16}\eta$$

which are the same as those of the reference 2).

The curved plate was divided into the elements as shown in Fig.14. The edge strip between the simply supported line and the free edge is also treated as a element in order to compare with the experimental results. In the case where both Dxs and Dys are not zero, the deformation is not strictly symmetrical about x and y axes. However, as the influence is considered to be not so important, it is treated as symmetrical about the x axis as an approximation and the region $y \leq 0$ alone is analysed. For the x direction, we have analysed all region taking into account the possibility that the anti-symmetric mode about the y axis may give an influence on the snap-through instability.

The geometrical boundary condition given in the half region analysis is as follows;

x=60 mm ; at the nodes except A;
u=const(= Ues), v=w=0, $\theta x=\theta y=0$
at the node A; u=const(= Ues)alone
x=-60 mm ; at the nodes except B;
u=v=w=0, $\theta x=\theta y=0$
at the node B; u=0 alone
y=0 mm ; v=0, $\theta x=0$
y=-60 mm ; w=0, $\theta y=0$ (29)

In the case if we analyse the one-fourth region $x \geq 0$ and $y \leq 0$ alone using a symmetrical condition about the y-axis, the geometrical condition is written as

x=0 mm ; u=0, $\theta y=0$ (30)

4.2 Calculated Results

The calculated results are drawnin Figs.7~13. Some of the deflection shape calculated are

shown in Fig.15. In the present FEM analysis under the boundary condition v=0 at x=±b/2, the deflection appears at the load lower than the buckling load under the condition of no initial imperfection. Namely, as the elongation in the y-direction due to Poisson's ratio under the compression in the x-direction is constrained at the upper and lower boundaries, the center of the panel has to deflect in the convex side under the boundary conditions w=0 at y=±b and free at y=±(b+ℓ).

For the panel 6p-1, the result of the FEM analysis up to 1200kgf shows a deflection in the convex side alone without a maximum point or instability. However, at the load about 720kgf the value of the determinant of the tangential stiffness matrix, which gives an indication of stability, has abruptly become 0.2×10^{-6} times of that of the previous step. However, the value of the determinant has not changed the sign and becomes a reasonable order again. Above the load the compressive stiffness has become lower with a kink as shown in Fig.7a. Fig.15a shows the deflection shape at the lines y=0mm and y=-15mm at two loads lower or higher than the load. Although the deflection shape along the y=0mm line is a simple wave, the deflection shape along the y=-15mm line varies from a simple wave to a higher mode wave. It is considered the decrease of the compressive stiffness is due to this variation of deflection shape. In the case 6p-1, the deflection shape is symmetrical for the x-axis because of Dxs=Dys=0.

In the load versus end-shortening relation of the case 6p-3, although a maximum point has appeared at P=360kgf, the value of P is an unique function of given end-shortening, then instability has not appeared in the FEM analysis different from the case 6p-2. The deflection of the y=0 line shown in Fig.15b is a pattern of two waves in the convex side at P=352kgf, which is much different from Eq.(7) as explained in the section 2.3. However, at P=592kgf the deflection is a simple wave in the concave side. The deflection shape is not symmetrical about the y-axis because of Dxs=0 and Dys=0.

In the case 8p-1, an instability due to bifurcation buckling to unsymmetrical mode has appeared at P=1270kgf. The case where the boundary condition for v at x=+b/2 is changed to be free is also calculated by the FEM analysis for comparison with the solution by the Galerkin method. The result is drawn in Fig.10. In this case the prebuckling deformation has been quite a small as a matter of course. A good agreement is observed between this FEM solution and the Galerkin method solution including the region of large deflection except a litte difference of buckling load in Fig.10a.

In the case 8p-2, the decrease of compressive stiffness has appeared taking P=1700kgf as a kink point. The deflection shapes calculated suggest that the reason of the decrease is the same as that explained in 6p-1.

In the case 8p-3, the prebuckling deformation to the convex side is large as shown in Fig.12a, because of large value of $\nu\alpha$. An instability has appeared at the maximum point P=1070kgf of the P versus Wc curve.

In the case 12p-1 also, the maximum instability point has apeared. However, the deflection at the convex side is large and the stress level is very high at the point.

The effective width ratio bm/b of the case 8p-1 calculated by the FEM analysis for the boundary condition v=0 at x=±b/2 is drawn in Fig.3. For comparison with the Galerkin solution it is calculated from

$$bm/b=a_{11}(P-P_\ell)/Ues \qquad (31)$$

where P_ℓ is the load carried at both edge strips. The comparison indicates that the effective width of the one-term Galerkin solusion is larger than that of the FEM solution, although the boundary condition is not same.

5. Comparison between Analytical and Experimental Results and Discussion

(1) Buckling Load

For the behavior of deformation before the snap-through, the experiment and the FEM solution are essentially different from the Galerkin solution because of the difference of the boundary condition. Although the buckling loads have been found by the δ^2 plot from the P~Wc relation for some of the experimental results and the FEM solutions and are shown in Table 1, a reasonable agreement between them is found only for 6p-1 and 8p-2 which are characterized by no snap-through in the FEM analysis. Therefore, it will be concluded that the so-called bifurcation buckling load is not clear in the boundary conditions of experiment.

(2) Snap-through Load

The snap-through load calculated by the FEM analysis is shown in Table 1. The values in parentheses in the case 6p-3 is not the snap-through load but the maximum point in the P versus Wc curve. Others are the load which makes the determinant of stiffness matrix equal to zero. In the cases 6p-2, 8p-1 and 8p-3 alone, good agreement is observed between the experiment and the FEM analysis. In the case 6p-1, a snap-through was measured in experiment different from the FEM solution. It will be concluded that the instability of deformed shape is sensitive to a small difference of the shape.

(3) P versus Wc Curve in Large Deflection

In the P versus Wc curves at large deflection after the snap-through of the cases 6p-2, 6p-3 and 8p-1 and in the P versus Wc curves of the cases 8p-2 and 12p-1, roughly good agreements are seen among the experimental results, the FEM solution and the Galerkin solution. The Galerkin solution has a tendency a little bit stiffer than the FEM solution at the region of large deflection after the snap-through because of one term approximation in the cases 6p-2, 6p-3 and 8p-1. The experimental deflection has a tendency to become rapidly larger than the FEM solution above a load close to the maximum load. It is considered this suggests that a local failure has started and it lowers the effective stiffness. In the cases 8p-3I and 8p-3II we cannot find a good agreement between the experimental result and the FEM solution.

(4) P versus Ues Relation

In the relation between P and Ues, a good agreement is observed between the Galerkin solution and the FEM solution in the state before the snap-through. However, at the state of post snap-through, except the case 8p-2 and 12p-1, distinct differences are seen between the Galerkin solution and the FEM solution in spite of good

agreement for the P versus Wc relation. It is considered that at the large deflection the shape of deformation transfers from a cosine type wave to the shape of a pan and the center deflection alone agrees well between them. Therefore, it is concluded that the Galerkin solution by one-term approximation is not sufficient for calculation of compressive stiffness at the post-buckling state.

The FEM solution for the P versus Ues relation does not show a good agreement with the experimental result except the case 6p-2. Particularly the difference is large in the state before the snap-through. In some cases the slop dP/dUes shows a good agreement between them at the state of the post snap-through.

(5) Influence of Lamination Constitution on the Maximum Load

In comparison with the experimental results the following properties can be stated. Among the six layer panels, although 6p-2 is the highest for the snap-through load, the maximum load of 6p-1 is much higher than that of 6p-2 and 6p-3. Among the eight layer panels, although the buckling load of 8p-2 is lower than the snap-through load of 8p-1, 8p-3Ⅰ and 8p-3Ⅱ, the maximum load of 8p-2 is higher than that of 8p-1, 8p-3Ⅰ and 8p-3Ⅱ. However, the difference between the maximum loads of 8p-2 and 8p-1 is small. These results may yield a conclusion that for the maximum load the laminates composed of 0° and 90° layers alone give higher values than that of the in-plane quasi-isotropic laminates. The ratio of the maximum load to the snap-through load is 2.70 for 6p-1, 1.62 for 6p-2, 1.51 for 6p-3, 1.65 for 8p-1, 1.47 for 8p-3I and 1.50 for 8p-3Ⅱ. The panel 12p-1 has two times lamination of 6p-2. Is is noticeable that 12p-1 yields 4.08 times maximum load of 6p-2.

6. Conclusion

It is considered that the present study by experiments, the FEM analysis and the Galerkin method about the seven types of laminated curved panels yields the following conclusion.

1) The experimental result and the FEM solution indicate that the curved panel deflects to the convex side from the beginning due to the boundary condition v=0 at loading edges and have the prebuckling deformations and instability behaviors which are different from the Galerkin method solution with the boundary condition Nxy=0 at the loading edges.

2) The post-buckling behavior until the final failure load can be divided into three categories; (a) the panel has a load carrying capability also after the snap-through to the concave side, (b) the final failure occurs in the convex side deflection without snap-through and (c) the final failure occurs right after snap-through. The property depends on the lamination constitution and the shape factor.

3) The curved panels with the width-thickness ratio and shape factor in the present study have a considerable load-carrying capability at the post-buckling state.

4) Roughly good agreements are seen between the experimental results and the FEM solution.

5) In the comparison under the condition of the same number of layers, the inplane quasi-isotropic curved panels yield a higher primary buckling load, while the lamination constitutions which consist mainly of 0°and 90°lamina with a small value of γ_{xy} yield a higher failure load.

Acknowledgement

The authors wish to express their gratitude to the Pioneering Research and Development Laboratories of TORAY Inc. for the preparation of the test specimens.

References

1) S. Kobayashi, K. Sumihara and M. Kihira; Compressive Buckling Strength of CFRP Laminated Panels (Part 1), Jour. Japan Soc. Aero. Space Scis., Vol.28, No.319, June 1980, pp.293-301.

2) K. Sumihara and S. Kobayashi; Compressive Buckling Strength of CFRP Laminated Panels (Part 2), Jour. Japan Soc. Aero. Space Scis., Vol.29, No.327, April 1981, pp.216-227.

3) K. Sumihara, S. Kobayashi and K. Koyama; Shear Buckling of CFRP Laminated Panels (1st Report), Jour. Japan Soc. Aero. Space Scis. Vol.29, No.329, June 1981, pp.321-332.

4) S. Kobayashi, K. Sumihara and K. Koyama; Shear Buckling Strength of Graphite-Epoxy Laminated Panels, "Composite Materials", K. Kawata and T. Akasaka Ed., Proc. Japan-U.S. Conference, Tokyo, 1981, pp.436-445.

5) Y. Hirano and T. Hayashi, Effective Width of Curved Plates (I)-Analysis, (Ⅱ)-Experiments, Bull, Inst. Space Aero. Sci., Univ. of Tokyo, Vol.3, No.3, July 1957, pp.449-475.

6) T. Hayashi and K. Kondo; On the Buckling Load and Postbuckling Behavior of Curved Panels under Axial Compression, Proc. 8th Int. Symp. Space Tech. Sci., Tokyo, 1969, pp.259-268.

7) Y. Zhang and F.L. Matthews; Postbuckling Behavior of Cylindrically Curved Panels of Generally Layered Composite Materials with Small Initial Imperfections of Geometry, "Composite Structures 2" edited by I.H. Marshall, 1983, p.428.

8) S. Kobayashi, H. Seko and K. Hirose; Compressive Buckling of CFRP Circular Cylindrical Shells,PartⅡ Optimum Constitution of Lamination, Jour. Japan Soc. Aero. Space Sci., Vol.32, No.362, March 1984, pp.180-186.

9) S. Kobayashi, K. Koyama, H. Seko and K. Hirose; Compressive Buckling of Graphite-Epoxy Composite Circular Cylindrical Shells, "Progress in Science and Engineering of Composites", T. Hayashi, K. kawata and S. Umekawa Ed., Proc. 4th Int. Conf. Comp. Mat., Oct. 1982, pp.555-564.

10) T. Ishikawa, K. Koyama and S. Kobayashi; Elastic Moduli of Carbon Composites and Carbon Fiber, Jour. Japan Soc. Aero. Space Scis., Vol.23, No.263, Dec. 1975, pp.678-684.

11) S. Kobayashi and T. Ishikawa; Elastic Moduli of Unidirectional Fiber-Reinforced Composites, Jour. Japan Soc. Aero. Space Scis., Vol.23, No.256, May 1975, pp.319-326.

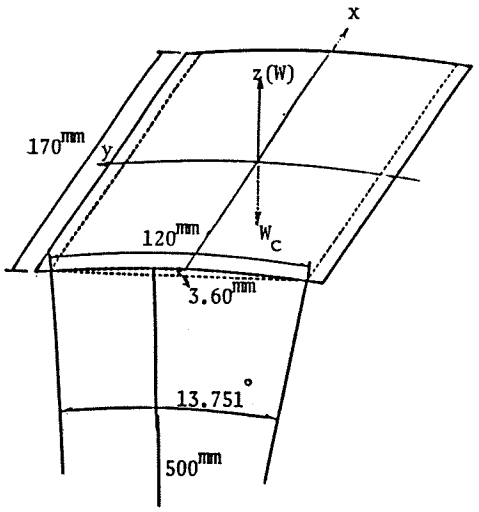

Fig.1 Curved plate, Dimensions

Table 1. Experimental and Calculated Results of Graphite-Epoxy Laminated Curved Panels

specimen	lamination constitution	thickness (mm)	buckling load (kgf)			snap-through load (kgf)		maximum load (kgf) (Exp.)
			Experiment	Galerkin method	F.E.M.	Experiment	F.E.M.	
6p-1	[0°90°0°/sym.]	0.708	297	300	331	(1) 612 (2) 672		1817
6p-2	[0°60°-60°/sym.]	0.723	–	521	545	732	* 691 663	1187
6p-3	[60°0°-60°/sym.]	0.701	–	† 464 401	305	682	(360)	1032
8p-1	[0°90°45°-45°/sym.]	0.948	–	778	* 818 835	1262	1270	2077
8p-2	[0°90°0°90°/sym.]	0.943	558	529	574	–	–	2102
8p-3 I	[45°-45°45°-45°/sym.]	0.976	–	612	* 583 506	(1)1087 (2) 847	* 1037 1070	– 1242
8p-3 II	[45°-45°45°-45°/sym.]	0.970	–	–	–	(1)1027 (2) 882 (3) 882	–	– – 1327
12p-1	[0°60°-60°0°60°-60°/sym.]	1.473	1520	1845	1922	4642	4400	4842

† ··· see section 2.3

* ··· Value obtained by the 1/4 region analysis.

able 2. Elastic Moduli of Graphite Fiber, Epoxy and Unidirectional Composites

A. Fiber, Torayca T300;

E_{fL}= 22000kgf/mm^2 , G_{fLT}= 2500kgf/mm^2

E_{fT}= 0.08xE_{fL} , ν_{fLT}= 0.30 , ν_{fTT}= 0.42

Epoxy, #2500;

E_m= 370kgf/mm^2 , ν_m= 0.36

B. Unidirectional Composites (V_f= 60%);

E_L= 13350kgf/mm^2 , E_T= 911.2kgf/mm^2

G_{LT}= 473.6kgf/mm^2 , ν_{LT}= 0.321 (ν_{TT}=0.519)

Table 4. Characteristic Values of Test Panels

specimen	μ		poisson's ratio (ν_x)	$Z=b^2/(Rt)$
6p-1	±4.3959	±0.3069	0.0318	40.68
6p-2	±1.0000	±1.0000	0.3124	39.83
6p-3	±1.0000	±1.0000	0.3124	41.08
8p-1	±1.0000	±1.0000	0.3124	30.38
8p-2	±3.8714	±0.2583	0.0411	30.54
8p-3 I	±0.4843	±0.8749i	0.7751	29.51
12p-1	±1.0000	±1.0000	0.3124	19.55

b=120mm , R=500mm

Table 3. Elastic Moduli of Test Laminates

specimen	a_{ij} (x10^{-4}) mm/kgf				Dij kgf·mm					
	a_{11}	a_{22}	a_{12}	a_{33}	Dxx	Dyy	Dxy	Dss	Dxs	Dys
6p-1	1.527	2.778	-0.088	29.823	301.6	123.2	8.72	14.01	0.	0.
6p-2	2.691	2.691	-0.841	7.063	315.0	95.8	30.07	35.70	9.98	27.98
6p-3	2.775	2.775	-0.867	7.285	138.8	178.8	55.82	60.95	27.29	76.51
8p-1	2.052	2.052	-0.641	5.387	608.5	358.4	47.29	59.98	20.84	20.84
8p-2	1.479	1.479	-0.061	22.391	665.9	337.7	20.60	33.10	0.	0.
8p-3I	6.094	6.094	-4.723	2.976	326.3	326.3	252.89	266.74	90.98	90.98
12p-1	1.321	1.321	-0.413	3.467	2061.6	1181.2	369.60	52.76	147.88	117.20

Table 5. Maximum Strains in Experiment
(unit; $\times 10^{-6}$)

specimen	load (kgf)	tensile strain	compressive strain
6p-1	1802	7503 (15)	7975 (12)
6p-2	1152	9375 (30)	5945 (4)
			6773 (38)
6p-3	1002	6837 (30)	6126 (4)
		6927 (7)	
8p-1	2002	6040 (26)	8334 (4)
8p-2	2102	13801 (14)	9580 (29)
8p-3 I	1202	15490 (15)	14149 (13)
			15114 (4)
8p-3 II	1302	17393 (31)	24778 (29)
12p-1	4602	* 12691 (27)	9097 (9)

* Maximum strain at P=4002 kgf above which the 27th gage had peeled off.

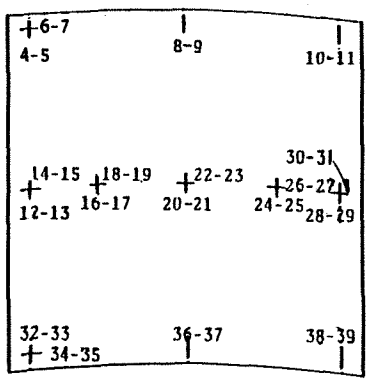

Fig.6
Position and Direction of Strain Gauge

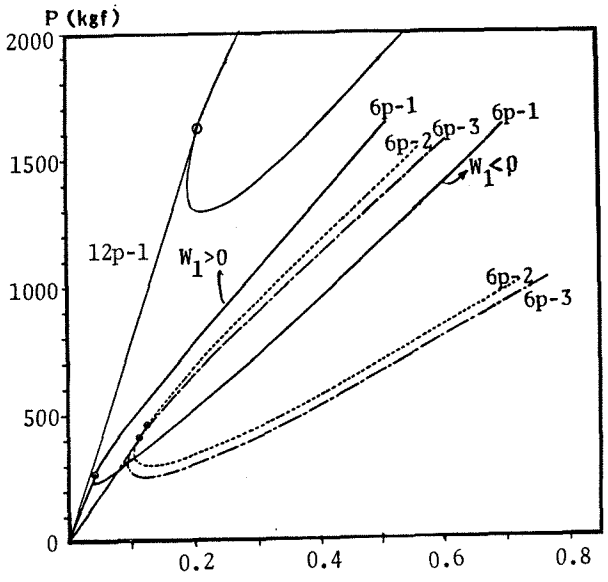

(a) Panels composed of six layers and twelve layers

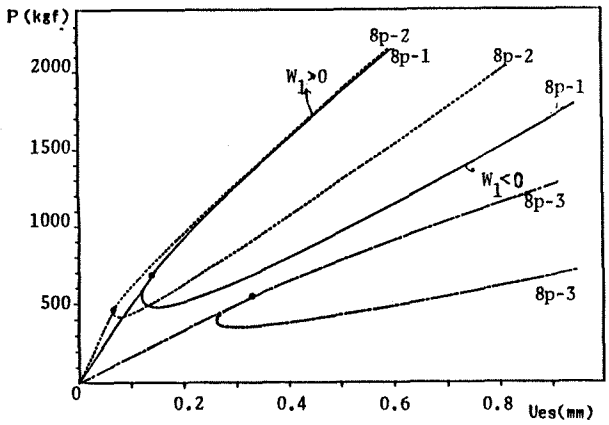

(b) Panels composed of eight layers

Fig.2. Load versus End-shortening Relation Calculated by the Galerkin Method
(Symbol ⊙ indicates the buckling load.)

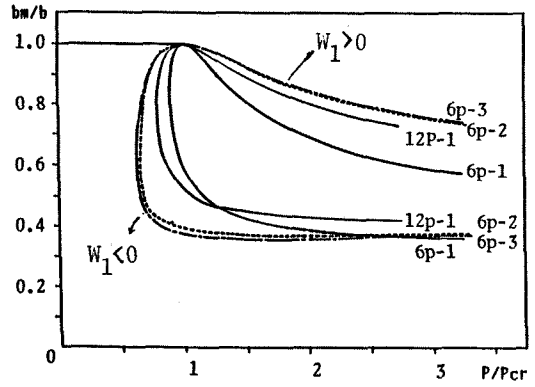

(a) Panels composed of six layers and twelve layers

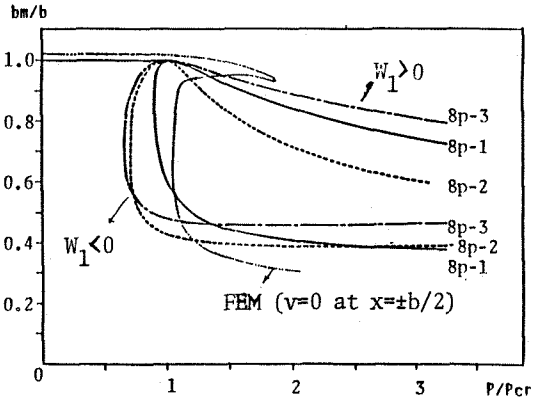

(b) Panels Composed of eight layers

Fig. 3. Load versus Effective Width Relation

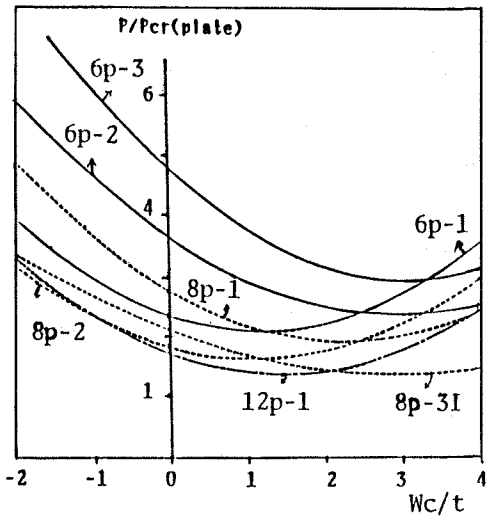

Fig.4 P/Pcr(plate) versus Wc/t Relation calculated by the Galerkin Method

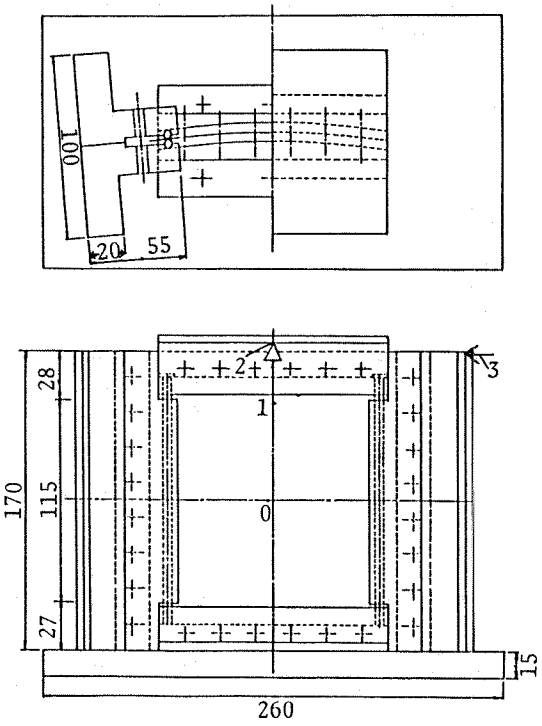

Fig.5 Test Set-up

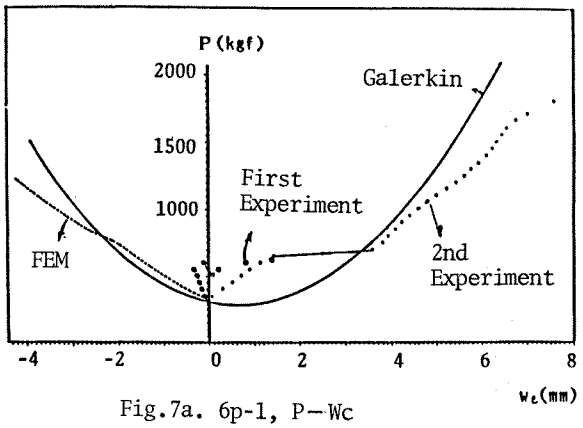

Fig.7a. 6p-1, P—Wc

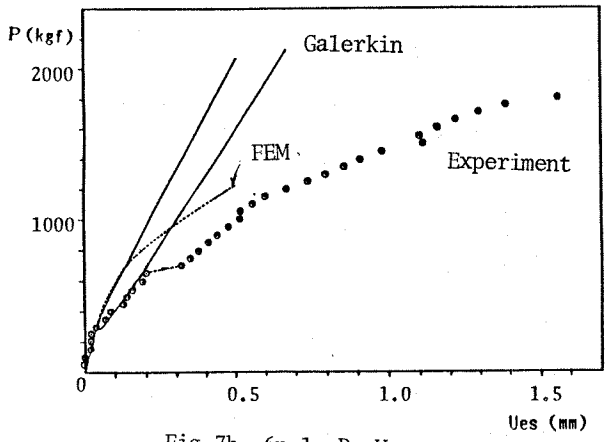

Fig.7b. 6p-1, P—Ues

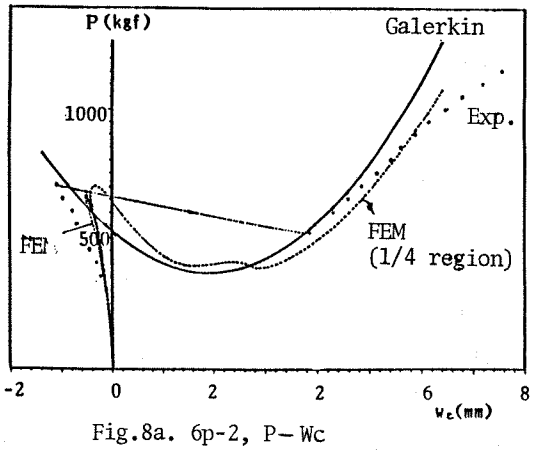

Fig.8a. 6p-2, P—Wc

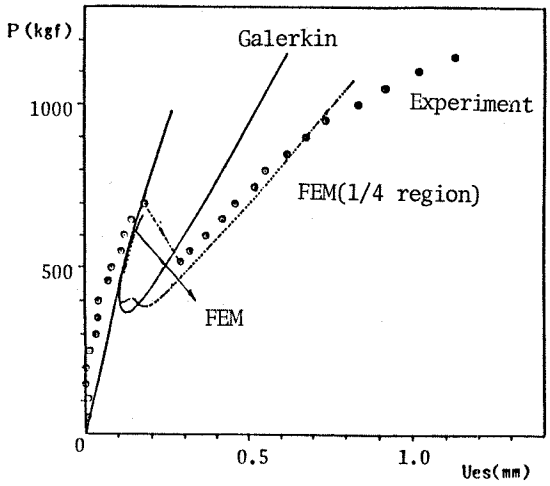

Fig.8b. 6p-2, P—Ues

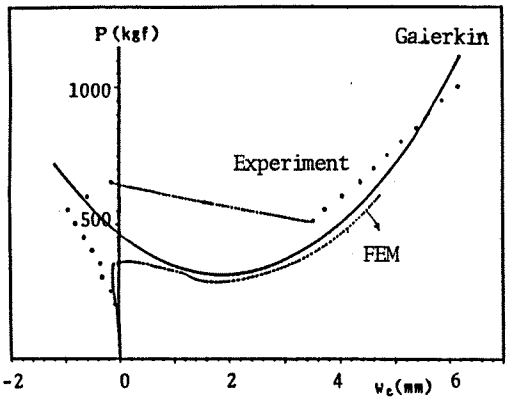

Fig.9a. 6p-3, P−Wc

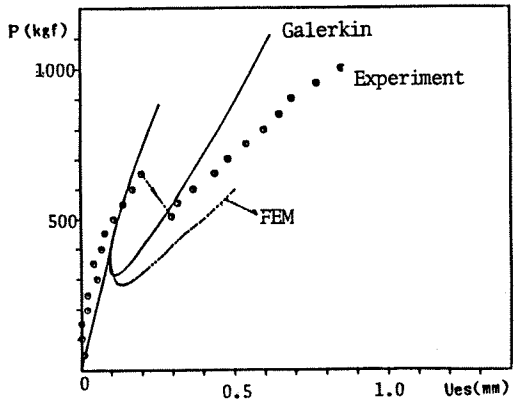

Fig.9b. 6p-3, P−Ues

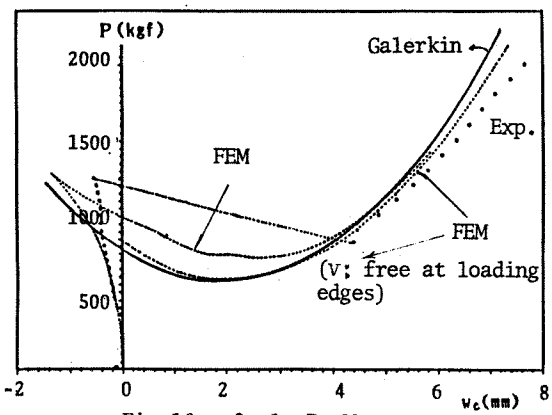

Fig.10a. 8p-1, P−Wc

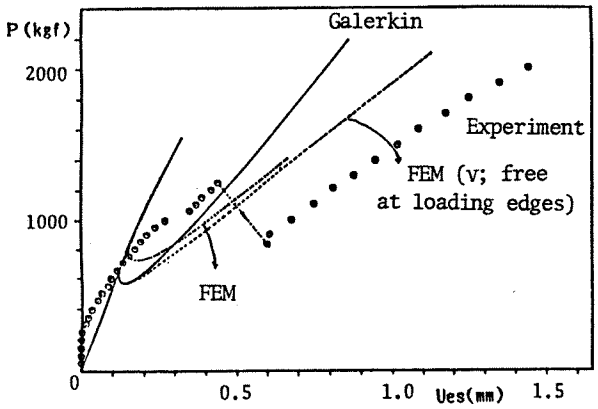

Fig.10b. 8p-1, P−Ues

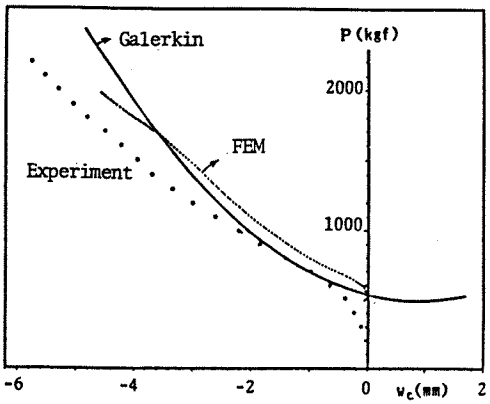

Fig.11a. 8p-2, P−Wc

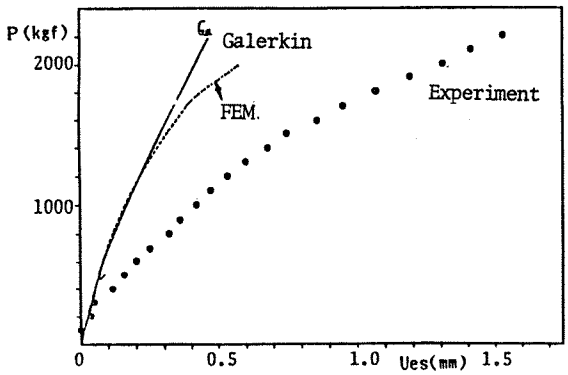

Fig.11b. 8p-2, P−Ues

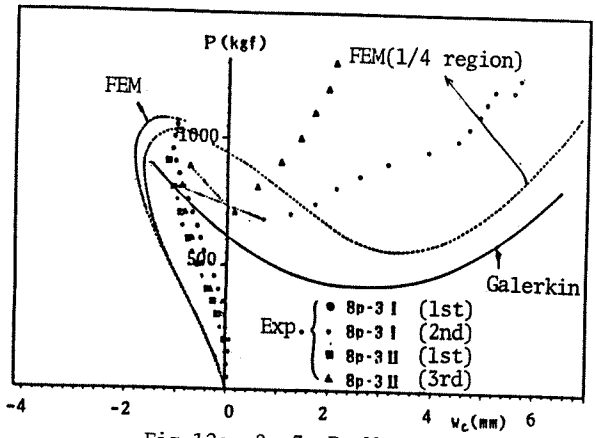

Fig.12a. 8p-3, P−Wc

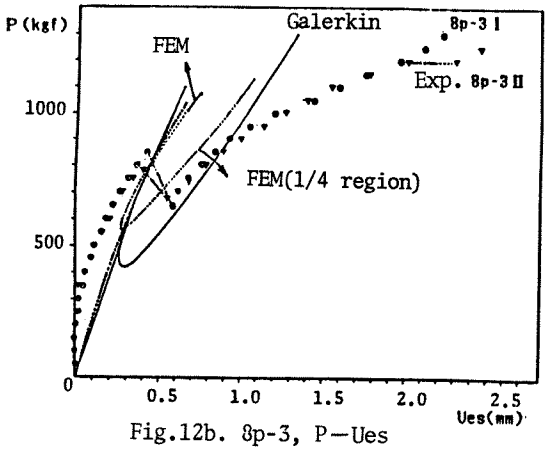

Fig.12b. 8p-3, P−Ues

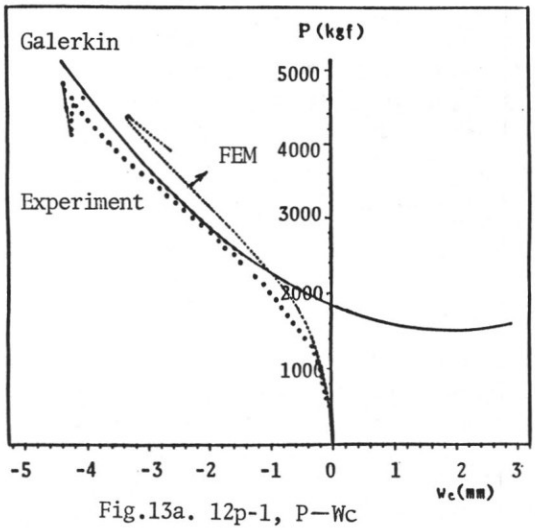

Fig.13a. 12p-1, P—Wc

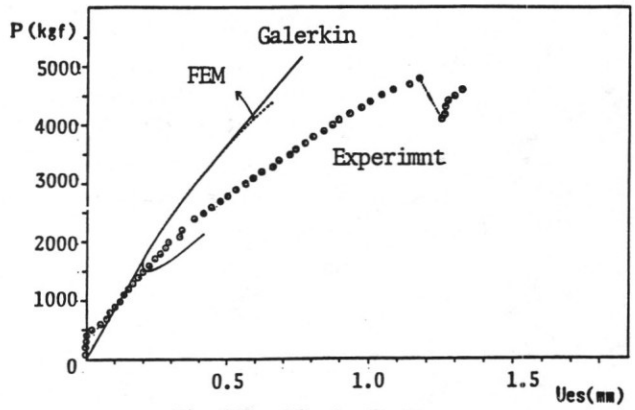

Fig.13b. 12p-1, P—Ues

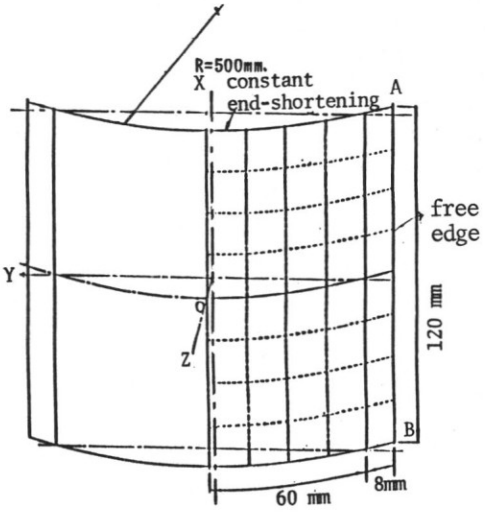

Fig.14. Division of Finite Element

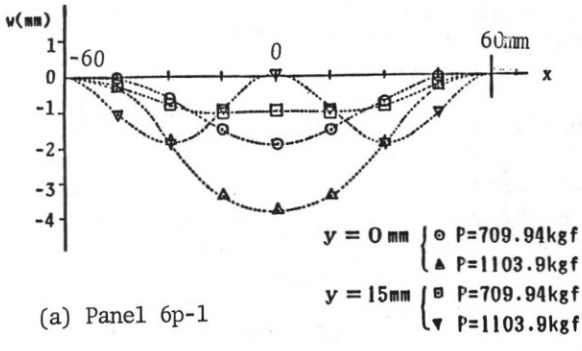

(a) Panel 6p-1

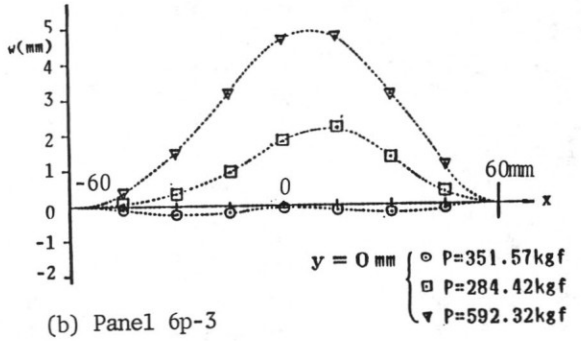

(b) Panel 6p-3

Fig.15. Shape of Deflection in the Section y=const. Calculated by FEM Analysis (W is positive in the concave side in this figure.)

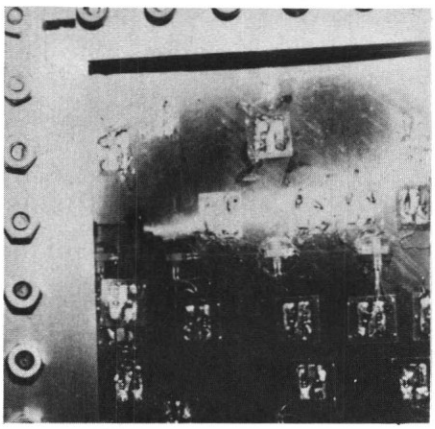

Photograph 1. 8p-1

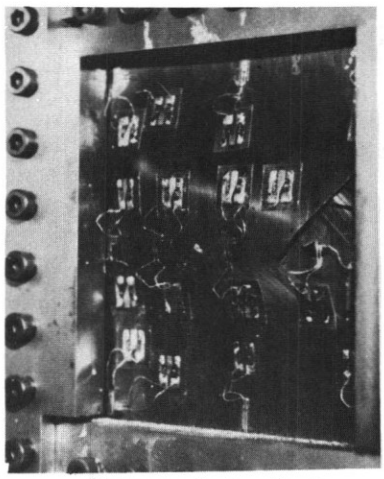

Photograph 3. 8p-2

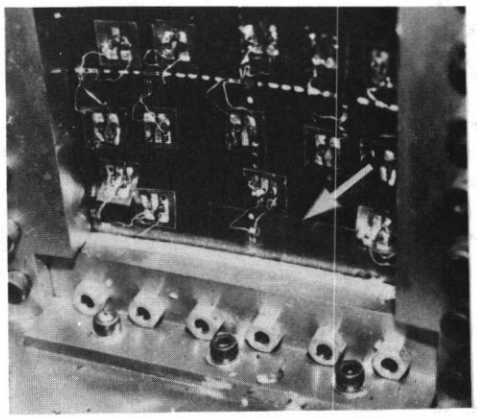

Photograph 2. 8p-3Ⅱ